Friction

Research Article

Robust superlubricity in encapsulated graphene nanoribbons through van der Waals confinement

Sen Wang[1], Wengen Ouyang[1,2,✉]

Cite this article: Wang S, Ouyang WG. *Friction* 2026, **14**: 9441242. https://doi.org/10.26599/FRICT.2026.9441242

ABSTRACT: The frictional behavior of encapsulated graphene nanoribbons is pivotal for enabling ultralong growth and ensuring the reliability of nanoelectronic devices, yet it remains elusive due to the buried nature of the interfaces. Using large-scale molecular dynamics simulations, we demonstrate that GNRs confined between hexagonal boron nitride (h-BN) layers exhibit friction forces over an order of magnitude lower than those of their on-surface counterparts. The kinetic friction force (F_k) scales sublinearly with length (L_{GNR}) as $F_k \propto (\ln(L_{GNR}))^3$. This robust superlubric state originates from interfacial registry competition with adjacent AA′-stacked h-BN layers, which inhibits coherent strain accumulation and suppresses stick-slip behavior, thereby promoting collective low-dissipation sliding. Furthermore, we reveal a negative differential friction coefficient versus confinement pressure as the number of h-BN layers increases, arising from the competition between pressure-induced ripple suppression and the monotonically enhanced h-BN/h-BN interlayer perturbations in thicker stacks. This interplay provides a practical avenue for tuning friction via confinement engineering. These findings elucidate atomistic dissipation pathways at buried van der Waals interfaces and establish encapsulation as a viable route to robust GNR-based nanoelectronics and scalable superlubric systems.

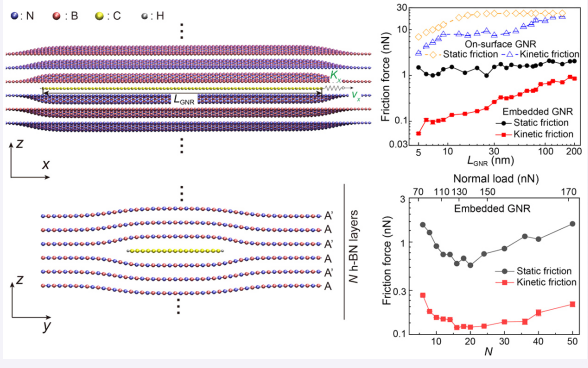

KEYWORDS: van der Waals (vdW) encapsulation; graphene nanoribbon (GNR); superlubricity; friction scaling law; interfacial registry competition

1 Introduction

Graphene nanoribbons (GNRs) exhibit exceptional electronic [1, 2] and mechanical properties [3], making them promising building blocks for nanoelectronic devices such as field-effect transistors (FETs), quantum circuits, flexible electronics, sensors, and thermoelectric generators [4–11]. However, despite progress in fabrication methods such as top-down cutting [12, 13], nanotube unzipping [14, 15], bottom-up chemical vapor deposition [6, 16–21], and on-surface synthesis [22–24], these approaches typically produce ribbons with a trade-off between length and width, poor chirality control, and structural nonuniformity [25–27], limiting their integration into high-performance devices. A recent breakthrough by Lyu et al. [28, 29] demonstrated the *in situ* growth of ultralong (0.25 mm), ultranarrow (< 5 nm), and homochiral zigzag (ZZ) GNRs within hexagonal boron nitride (h-BN) stacks. This approach enabled the transfer-free fabrication of embedded GNR FETs with outstanding performance—mobilities up to ~4,600 $cm^2 \cdot V^{-1} \cdot s^{-1}$ and on/off ratios of ~10^6. This advance not only stimulated broad interest and attention [30–34] but also revealed that the friction at the embedded interface is a decisive factor controlling ultralong growth and chirality selection.

Although the tribological behavior of surface-supported GNRs has been extensively studied, including superlubricity [35, 36], edge effects [36], length dependence [37–39], and morphological evolution [40], the frictional behavior of fully encapsulated GNRs remains largely unexplored. Unlike surface-supported ribbons, an encapsulated GNR is simultaneously in contact with two adjacent layers, where van der Waals (vdW) confinement can fundamentally alter the mechanical [41–43], frictional [44–46], electronic [47–50], and thermal transport [51–55] behavior of layered heterostructures and related devices. Frictional forces at embedded interfaces can drive wear, strain accumulation, and dissipation while also strongly coupling to electronic and thermal transport [56–61]. Clarifying the microscopic mechanisms of encapsulated GNR friction is therefore essential for advancing fundamental tribology as well as for enabling the design of reliable nanoscale devices [62–66] and the aforementioned homochiral ultralong GNR growth.

[1] Department of Engineering Mechanics, School of Civil Engineering, Wuhan University, Wuhan 430072, China. [2] State Key Laboratory of Water Resources Engineering and Management, Wuhan University, Wuhan 430072, China.

✉ Corresponding author. E-mail: w.g.ouyang@whu.edu.cn

Received: October 10, 2025; Revised: February 27, 2026; Accepted: March 9, 2026

In this work, we employ large-scale molecular dynamics (MD) simulations with state-of-the-art force fields [67, 68] to systematically investigate the frictional behavior of GNRs embedded between h-BN layers. We show that encapsulation reduces friction by over an order of magnitude compared with surface-supported GNRs. Furthermore, we identify a consistent slow sublinear scaling of friction with nanoribbon length that persists across a wide range of sliding velocities, confirming the manifestation of robust superlubricity. This ultralow friction state originates from registry competition with adjacent AA′-stacked h-BN layers, which suppresses strain accumulation and prevents localized stress, enabling smooth collective sliding instead of soliton-mediated stick-slip. Finally, we demonstrate that the number of h-BN encapsulation layers provides a practical route to tune friction through vdW confinement pressure. Together, these findings establish encapsulation as a powerful mechanism for achieving controllable superlubricity, clarify the role of buried interfaces in enabling ultralong GNR growth, and provide design principles for robust, durable, and energy-efficient GNR-based nanoelectronic systems.

2 Model setup

Our model system consists of armchair (AC)- and ZZ-GNRs encapsulated within six layers of AA′-stacked h-BN (Fig. 1). The GNRs were aligned along the AC (ZZ) direction of the h-BN lattice for AC-GNRs and ZZ-GNRs, with lengths (L_{GNR}) ranging from 5 to 200 nm and a fixed width of ~2 nm. The ribbons were passivated with hydrogen at the edges. Periodic boundary conditions were applied in the x and y directions, while an open boundary condition was used in the z direction, with a 2 nm vacuum spacing. The lateral dimensions of the simulation box were set as (L_{GNR} + 8) nm × 12 nm to avoid interaction between periodic images.

The intralayer interactions within the GNR and h-BN layers were described using the second-generation reactive empirical bond order (REBO) potential [69] and the Tersoff potential [70], respectively. Interlayer interactions, including those between h-BN layers and between GNR and h-BN, were described via the registry-dependent interlayer potential (ILP) [39, 68, 71–74] with refined parameterization [39]. This state-of-the-art ILP captures the registry-dependent sliding energy corrugation by explicitly accounting for short-range Pauli repulsion [68], making it the current tool-of-choice for describing the anisotropic nature of weak and long-range vdW interactions in layered systems. The ILP has been extensively validated across various vdW heterostructures for characterizing structural reconstruction [47, 72, 75], thermal transport [51–53], mechanical [71, 76], and frictional [67, 77, 78] properties, as well as for simulating the growth of quasi-one-dimensional materials [28, 79]. While these empirical hybrid force fields perform robustly for pristine lattices, we acknowledge that their accuracy may decrease in nonideal systems featuring edges or defects. Such limitations could be addressed in future work by adopting a hybrid framework that combines single-layer machine-learned potential (sMLP) with a reparameterized ILP [80]. All simulations were carried out using the large-scale atomic/molecular massively parallel simulator (LAMMPS) package [81].

Prior to the sliding friction simulations, the system was fully relaxed to eliminate residual stress from GNR insertion. The whole system was equilibrated at 10 K and zero pressure for 100,000 steps with a time step of 1 fs, where the pressure was controlled by the Nosé–Hoover barostat. Then, the system was further optimized using the fast inertial relaxation engine (FIRE) algorithm with a threshold force value of 10^{-6} eV·Å^{-1}, followed by 10 iterative cycle combinations of the conjugate gradient (CG) and box/relax algorithm with a force convergence criterion of 10^{-4} eV·Å^{-1}. A final optimization using the FIRE algorithm was performed with a threshold force value of 10^{-6} eV·Å^{-1}. This relaxation induced a spindle-shaped deformation of the h-BN layers, where the layers are locally pushed apart by the presence of the GNR and then gradually recover their equilibrium interlayer spacing (~3.3 Å) at regions away from it (Fig. 1), consistent with previous experimental observations [28].

Subsequently, damped sliding friction simulations were carried out at 0 K under the NVE ensemble with a time step of 1 fs. The rightmost carbon atoms of the GNR were connected to a driving stage via parallel lateral springs, where the stage moved at a constant velocity of V_x = 1 m·s^{-1} along the x direction. The overall spring stiffness was fixed at $K_x = 100$ N·m^{-1} [82], yielding an atomic spring constant of $k_x = K_x/n$ for each dragged spring, where n is the total number of dragged atoms. Tests with a reduced stiffness of 30 N·m^{-1} confirmed that the qualitative frictional behavior remained unchanged (Fig. S1 in the Electronic Supplementary Material (ESM)). The far-edge regions of the h-BN slab (highlighted by red boxes in Fig. 1(a)) were held fixed as rigid boundaries. To dissipate heat generated during sliding, a Langevin thermostat damping ($\eta = 1$ ps^{-1}) was applied to the atoms in the outermost h-BN layers (top layer L6 and bottom layer L1 in Fig. 1(b)) [83–85]. The lateral spring force on each dragged carbon atom is given by Eq. (1):

$$F_i(t) = k_x\left(x_i(t) - X^{\text{stage}}(t)\right) \tag{1}$$

where $X^{\text{stage}}(t)$ and $x_i(t)$ are the instantaneous position of the driving stage and the i^{th} carbon atom in the driving GNR edge, respectively. The total lateral force acting on the GNR was then calculated as $F_L(t) = \sum_{i=1}^{n} F_i(t)$.

For comparison, we also performed friction simulations of on-surface GNRs using the same setup, except that the top h-BN trilayer stack was removed and only the bottom h-BN layer was thermostatted (Fig. S2 in the ESM). Furthermore, we performed

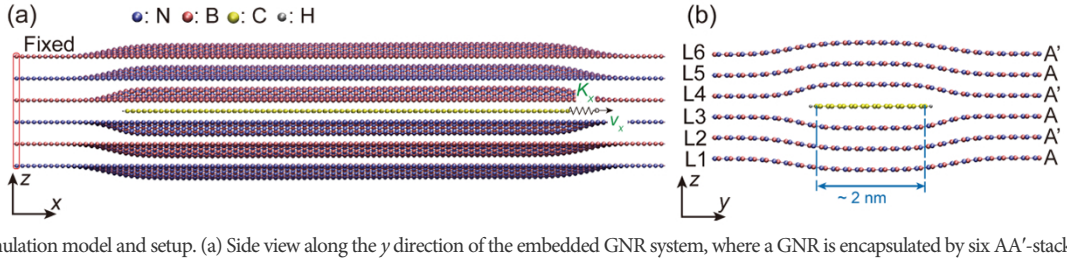

Fig. 1 MD simulation model and setup. (a) Side view along the y direction of the embedded GNR system, where a GNR is encapsulated by six AA′-stacked h-BN layers. The atoms in the red highlighted regions are fixed during sliding. (b) Cross-sectional view along the x direction of the simulation model. The rightmost carbon atoms of the GNR were attached via springs to a stage moving at a constant velocity $V_x = 1$ m·s^{-1}. The width of the GNR is fixed at ~2 nm, while its length varies from 5 to 200 nm. Mauve, blue, yellow, and gray spheres represent boron, nitrogen, carbon, and hydrogen atoms, respectively.

friction simulations for 30-nm-long GNRs embedded between h-BN stacks of varying thicknesses using the same setup as the six-layer system. In all these thickness-dependent simulations, the damping layers were consistently applied to the topmost and bottommost h-BN layers.

3 Results and discussion

Figure 2(a) shows representative lateral force traces for an embedded h-BN/GNR/h-BN (L_{GNR} = ~71 nm) system, revealing that AC-GNRs undergo stick-slip motion, whereas ZZ-GNRs exhibit smooth sliding, both with a characteristic period of ~2.3 Å (Fig. S3 in the ESM). The kinetic friction force was obtained by averaging the lateral force over multiple steady-state sliding periods, while the maximum lateral force over the entire trace was defined as the static friction force. Statistical errors in the kinetic friction were estimated from ten independent data sets, each spanning one sliding period. The kinetic friction (0.35 nN) of the embedded ZZ-GNR is ~1.5 times smaller than that of its AC-GNR counterparts (0.55 nN), consistent with our earlier findings [28]. This difference originates from the larger lateral displacements and greater deformation experienced by the AC-GNR as it navigates around local high-energy barriers (Section S4 in the ESM for details). Representative lateral force traces for on-surface GNRs (L_{GNR} = ~71 nm) are presented in Fig. 2(b). Both AC- and ZZ-GNRs exhibit pronounced stick-slip behavior, with nearly identical kinetic friction forces (12.9 nN for AC-GNRs and 13.4 nN for ZZ-GNRs). The sliding dynamics closely resemble those reported in our previous work [39]. Importantly, both the static and kinetic friction forces of on-surface GNRs are over an order of magnitude higher than those of embedded GNRs.

To further elucidate the interfacial frictional behavior of embedded GNRs, we investigate the dependence of the static and kinetic friction forces on the ribbon length (L_{GNR}) for both AC-GNRs and ZZ-GNRs. As demonstrated in Figs. 2(c) and 2(d), both forces increase sublinearly with L_{GNR} in the range of 5–200 nm. The static friction approximately doubles for AC-GNRs (red curves) and triples for ZZ-GNRs (black curves), following a scaling relation of $\sim 0.6(L_{GNR}/L_0)^{0.25}$, where $L_0 = 1\,\mathrm{nm}$. The kinetic friction (F_k) rises from ~0.1 to ~0.8 nN for both edge types, following the scaling law:

$$F_k \approx 0.005(\ln(1+L_{GNR}/L_0))^3 \quad (2)$$

Notably, the static friction of embedded GNRs exhibits periodic oscillations with length, arising from incomplete moiré patterns at the ribbon edges [86].

In contrast, on-surface GNRs display friction forces that are consistently over an order of magnitude higher. Their static friction (blue and orange curves in Fig. 2(c)) grows linearly with length before saturating beyond $L_{GNR} \approx 20$ nm, reaching plateaus of ~22.5 nN for the AC-GNRs and ~20.7 nN for the ZZ-GNRs. The kinetic friction (blue and orange curves in Fig. 2(d)) continues to increase with length, rising from ~2 up to ~16 nN for

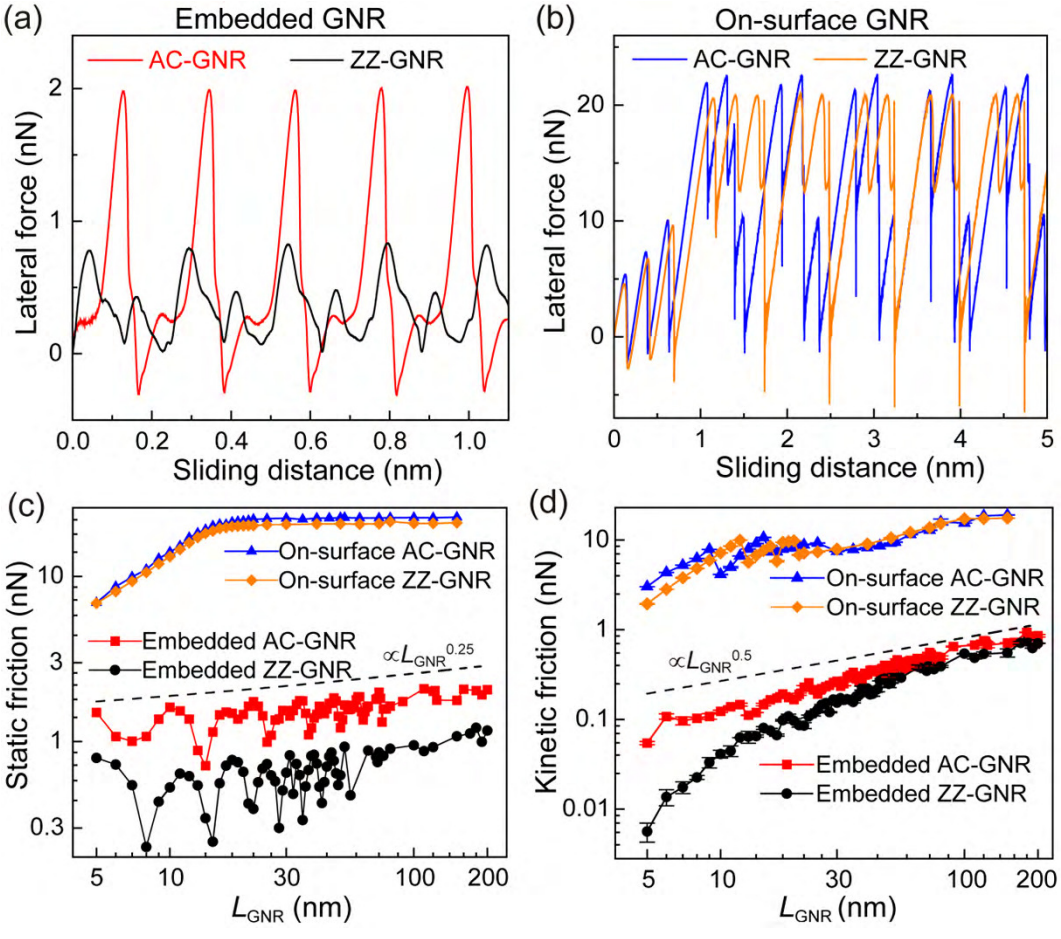

Fig. 2 Lateral force traces and length dependence of friction forces. Typical lateral force traces for (a) embedded and (b) on-surface GNRs with a length of ~71 nm. (c) Static and (d) kinetic friction forces of embedded and on-surface AC-GNRs and ZZ-GNRs with different L_{GNR}. The dashed lines indicate sublinear power-law scaling of friction with length.

both AC- and ZZ-GNRs, with a scaling law of $\sim 1.5(L_{GNR}/L_0)^{0.5}$. Extrapolation of the above scaling laws predicts an intersection of the static friction of embedded and on-surface GNRs at a ribbon length of ~1,400 μm, whereas the kinetic friction of embedded GNRs increases more slowly with length than that of on-surface GNRs and therefore remains consistently lower. These results highlight that h-BN encapsulation yields robust superlubricity in h-BN/GNR/h-BN heterostructures compared to their on-surface counterparts.

To investigate the effects of sliding velocity and temperature on frictional behavior, additional simulations were performed at both 0 K and room temperature under driving velocities of 0.5, 2, and 5 m·s^{-1}, as well as under quasi-static conditions. These tests confirm that the frictional trends reported for $V_x = 1$ m·s^{-1} are preserved across the explored velocity range at both temperatures (Figs. S6–S8 in the ESM). Notably, both the static and kinetic friction forces of the GNR increase with sliding velocity but decrease with rising temperature due to thermal activation effects. Despite these variations, the embedded h-BN/GNR/h-BN system maintains its robust superlubric state under all conditions examined (Figs. S6–S8 in the ESM). Collectively, these results indicate that our findings obtained at 0 K and V_x = 1 m·s^{-1} are relevant and applicable to realistic experimental scenarios. Further simulations with varying ribbon geometries and chiralities, including AC-GNRs with widths of $w = 0.7$ and 4.1 nm (Fig. S9 in the ESM), as well as atomically precise chiral GNRs with indices (3, 1, 8) [87, 88] (Fig. S10 in the ESM), reveal that while the friction magnitudes may vary with geometry and edge structure, the fundamental frictional scaling behavior remains preserved across all cases.

To elucidate the origin of the distinct sliding frictional behaviors in embedded and on-surface GNR systems, we analyzed the evolution of stress and strain distribution along the sliding direction (σ_{xx} and ε_{xx}) together with the bond-length evolution, displacement dynamics, and local registry index (LRI) [89, 90], using a 71-nm-long AC-GNR as a representative case (Fig. 3 and Figs. S12–S16 in the ESM). Here, σ_{xx} and ε_{xx} characterize the deformation of the GNR along the sliding direction, while the LRI quantifies the degree of local commensurability between the GNR and the h-BN layers, with lower values indicating stronger

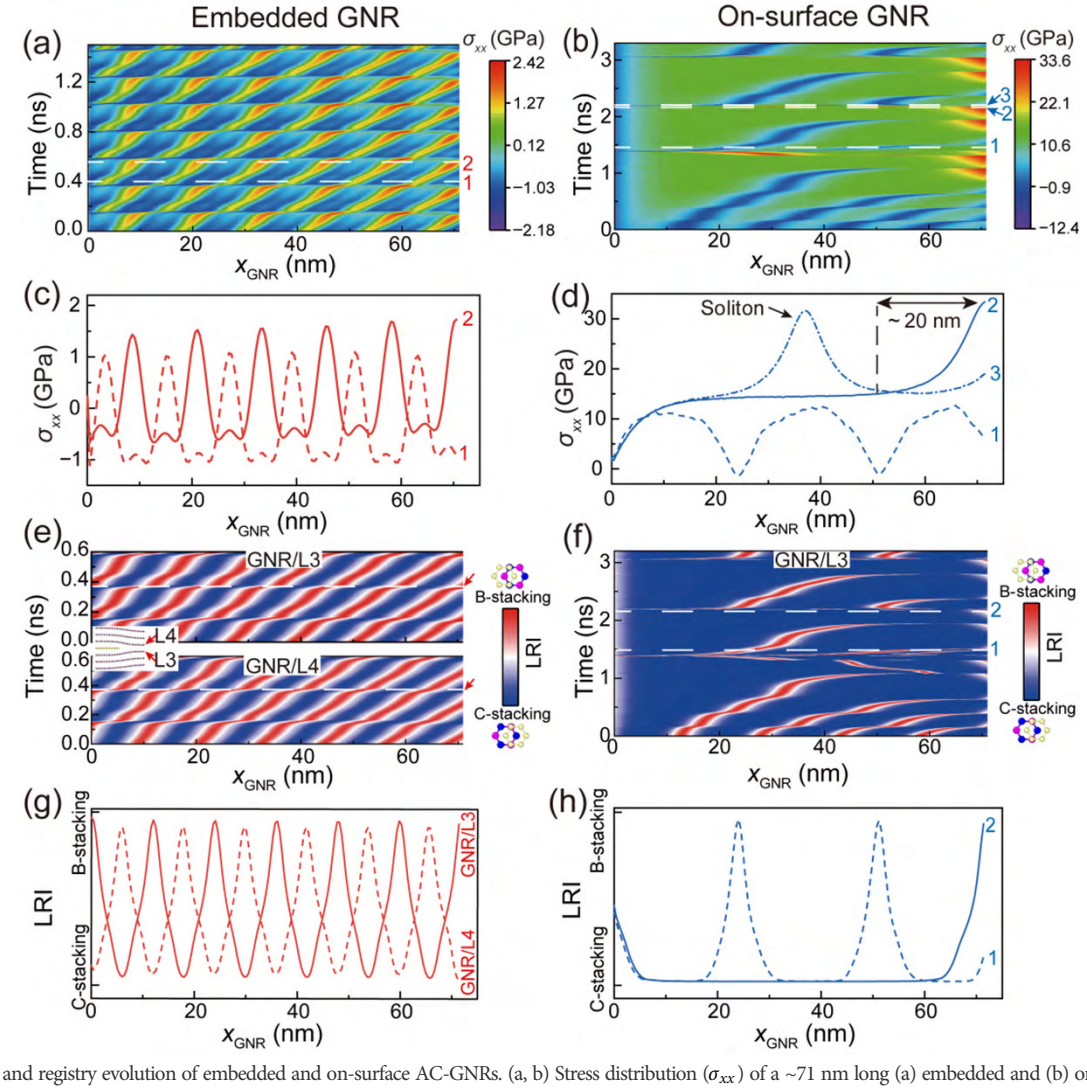

Fig. 3 Stress and registry evolution of embedded and on-surface AC-GNRs. (a, b) Stress distribution (σ_{xx}) of a ~71 nm long (a) embedded and (b) on-surface GNR during sliding. (c, d) Cross-sectional profiles along the dashed lines in panels (a) and (b). Panel (d) highlights the localized tensile stress near the leading edge, with a characteristic penetration length of ~20 nm, as well as the emergence of a stress soliton. (e, f) Local registry index (LRI) evolution for the embedded GNR with adjacent h-BN layers L3 and L4 (the positions of L3 and L4 are indicated in the inset of panel (e)). (g, h) Cross-sectional LRI profiles along the dashed lines in panels (e) and (f). Panel (g) illustrates the registry dislocation between GNR/L3 and GNR/L4. Both σ_{xx} and LRI are calculated by averaging the per-atom stress/LRI values along the narrow dimension of the GNR (excluding the passivating hydrogen atoms) and over a single axial unit cell. The position of each axial unit cell along the GNR (x_{GNR}) is calculated as the distance of its center-of-mass from the trailing edge of the ribbon. See more details in Section S8 of the ESM.

commensuration. Further calculation details are provided in Section S8 in the ESM.

In the encapsulated GNR configuration, σ_{xx} and ε_{xx} at the leading edge rise only slightly during sliding and decay smoothly and nearly linearly toward the trailing edge (Figs. 3(a) and 3(c) and Figs. S12 and S13 in the ESM). This nearly uniform stress distribution originates from registry competition between the GNR and the two adjacent AA′-stacked h-BN layers (L3 and L4 marked in the inset of Fig. 3(e)), as shown in Figs. 3(e) and 3(g) and Fig. S14 in the ESM. The GNR can align with the upper layer only by misaligning with the lower layer, and vice versa. This continual dislocation prevents the GNR from achieving full commensuration with either interface, thereby limiting elastic strain accumulation. As a result, the embedded GNR undergoes collective sliding with only minor fluctuations, accompanied by transient moiré patterns at the edges (Movie S1 and Figs. S15 and S16 in ESM). The total sliding barrier (ΔE_{tot}) remains low and is dominated by small variations in interlayer potential energy (ΔE_{int}) rather than stored elastic strain energy ($\Delta E_{\mathrm{el}}^{\mathrm{GNR}}$) (Fig. S17 and Table S1 in the ESM). Consequently, embedded GNRs exhibit ultralow, gradually increasing friction without saturation in the studied length range.

In contrast, a GNR sliding on a single-sided h-BN substrate develops a sharp stress and strain concentration at the leading edge, with σ_{xx} reaching 33.6 GPa (Figs. 3(b) and 3(d) and Figs. S12 and S13 in the ESM). Sliding proceeds via soliton-mediated stick-slip events, accompanied by pronounced tail-swing dynamics (Fig. 3(d) and Movie S2 in the ESM), consistent with earlier studies [38, 91, 92]. During the stick phase, C–C bonds stretch from the equilibrium 1.42 Å to 1.436 Å across most of the ribbon and up to 1.459 Å at the leading edge (Fig. S15 in the ESM). This elongation reduces the lattice mismatch with the substrate (the equilibrium B–N bond length is 1.446 Å) and promotes local commensuration (Figs. 3(f) and 3(h) and Fig. S14 in the ESM). This process enables substantial elastic energy storage while the leading edge advances and the trailing edge remains pinned (Fig. S16 in the ESM), which is abruptly released during slip events (Figs. 3(b) and 3(d) and Figs. S12 and S13 and Movie S2 in the ESM). The corresponding ΔE_{tot} is thus an order of magnitude higher than in the embedded case (Fig. S17 and Table S1 in the ESM), indicating the dominance of strain energy over interlayer potential variations. Stress relaxation follows an exponential decay with a characteristic penetration length of ~20 nm. For ribbons longer than this threshold, static friction saturates because only the leading segment of the GNR resists motion. For shorter GNRs, stress decays linearly from the leading to the trailing edge rather than forming a localized concentration (Fig. S20 in the ESM), leading to a linear friction-length relation.

Overall, embedded GNRs achieve smooth, low-friction sliding by suppressing stress localization through interfacial registry competition. In contrast, on-surface GNRs accumulate localized strain, which leads to higher static and kinetic friction, pronounced stick-slip oscillations, and soliton-driven slip events. This difference in strain accumulation drives distinct evolutions of the moiré pattern (Fig. S17 in the ESM). However, the Moiré evolution is a geometric manifestation of changing local registry, not an independent source of friction (Section S10 in the ESM). Moreover, no interfacial covalent bonding forms between the GNR and h-BN layers (Fig. S19 in the ESM).

To better understand the kinetic friction contrast between embedded and on-surface configurations, we analyzed the system's energy dissipation and its directional decomposition (Section S12 for details). The real-time dissipation power of atom j in the dissipative h-BN layers is calculated as Eq. (3):

$$p_{\mathrm{diss},\alpha}^{j}(t)=\eta m_j\left(v_{\alpha}^{j}(t)\right)^2, m_j=m_{\mathrm{B}}\ \text{or}\ m_{\mathrm{N}} \tag{3}$$

where $v_{\alpha}^{j}(t)$ is the velocity component of atom j in direction α ($\alpha=x,y,z$), η is the damping coefficient, and m_{B} and m_{N} are the atomic masses of boron and nitrogen atoms, respectively. The total instantaneous dissipation power of atom j is given by Eq. (4):

$$p_{\mathrm{diss}}^{j}(t)=\sum_{\alpha=x,y,z}p_{\mathrm{diss},\alpha}^{j}(t) \tag{4}$$

By averaging $p_{\mathrm{diss}}^{j}(t)$ over multiple sliding periods, the time-averaged energy dissipation power $\langle p_{\mathrm{diss}}^{j}\rangle$ is obtained. The total real-time dissipation power of the entire system and its directional dissipation components are expressed as Eq. (5):

$$P(t)=\sum_{j=1}^{n_{\mathrm{diss}}}p_{\mathrm{diss}}^{j}(t) \tag{5}$$

where n_{diss} is the total number of atoms in the damping layers. The time-averaged total dissipation power $\langle P\rangle$ and its directional components $\langle P_{\alpha}\rangle$ were obtained by averaging multiple sliding periods at the steady state.

Dissipation in embedded GNRs is overwhelmingly out-of-plane, whereas in on-surface GNRs, it is distributed across both out-of-plane (z) and in-plane (x, y) channels (Fig. S21 in the ESM). Mechanistically, embedded GNRs dissipate energy via moiré creep driven by out-of-plane relaxation, while on-surface GNRs exhibit mixed in-plane/out-of-plane dissipation associated with the formation and release of strain solitons (Fig. S22 and Movies S1 and S2 in the ESM). Phonon-spectrum analysis further supports this picture (Fig. S23 in the ESM). The embedded system dissipates primarily through low-frequency, out-of-plane washboard modes, characterized by the washboard frequency $f_{\mathrm{wb}}=V_x/a$ [93–95], where a is the lattice constant of h-BN along the armchair direction. In contrast, the on-surface system activates a broader spectrum of higher-frequency in-plane and out-of-plane modes associated with solitonic edge dynamics and vigorous interfacial rearrangements.

The length dependence of kinetic friction in both configurations stems from how the dissipation region scales with ribbon size. The spatial distribution of the time-averaged per-atom dissipation power $\langle p_{\mathrm{diss}}^{j}\rangle$ of the damped layers [96, 97] reveals that energy is mainly dissipated in the h-BN layers beneath the GNR, with pronounced hotspots near the GNR edges (Fig. S22 in the ESM). This feature is common to both on-surface and embedded configurations. As the ribbon length increases, more atoms participate in dissipation, and the total kinetic friction rises nearly proportionally with length. In short, longer GNRs generate larger dissipation regions, leading to higher overall friction.

For embedded GNRs, the h-BN encapsulation layers exert a vdW pressure arising from a balance between interlayer vdW interactions and elastic deformation of both the GNRs and the h-BN stack [98–101]. This pressure increases with the number of h-BN encapsulation layers (N), as shown in Fig. S24 in the ESM. To assess its effect on friction, we performed friction simulations for 30-nm-long GNRs embedded between h-BN stacks of varying thickness. The results reveal a nonmonotonic dependence of friction on N: Both static and kinetic friction decrease initially, reaching a minimum at ~16 layers, and then rise again (Figs. 4(a) and 4(b)). Specifically, the kinetic friction drops by ~54% for AC-GNRs (from ~0.26 to ~0.12 nN) and by ~67% for ZZ-GNRs (from ~0.15 to ~0.05 nN) as N increases from 6 to 16 (with the vdW encapsulation normal load increasing from ~80 to ~130 nN). Beyond this point, further encapsulation gradually

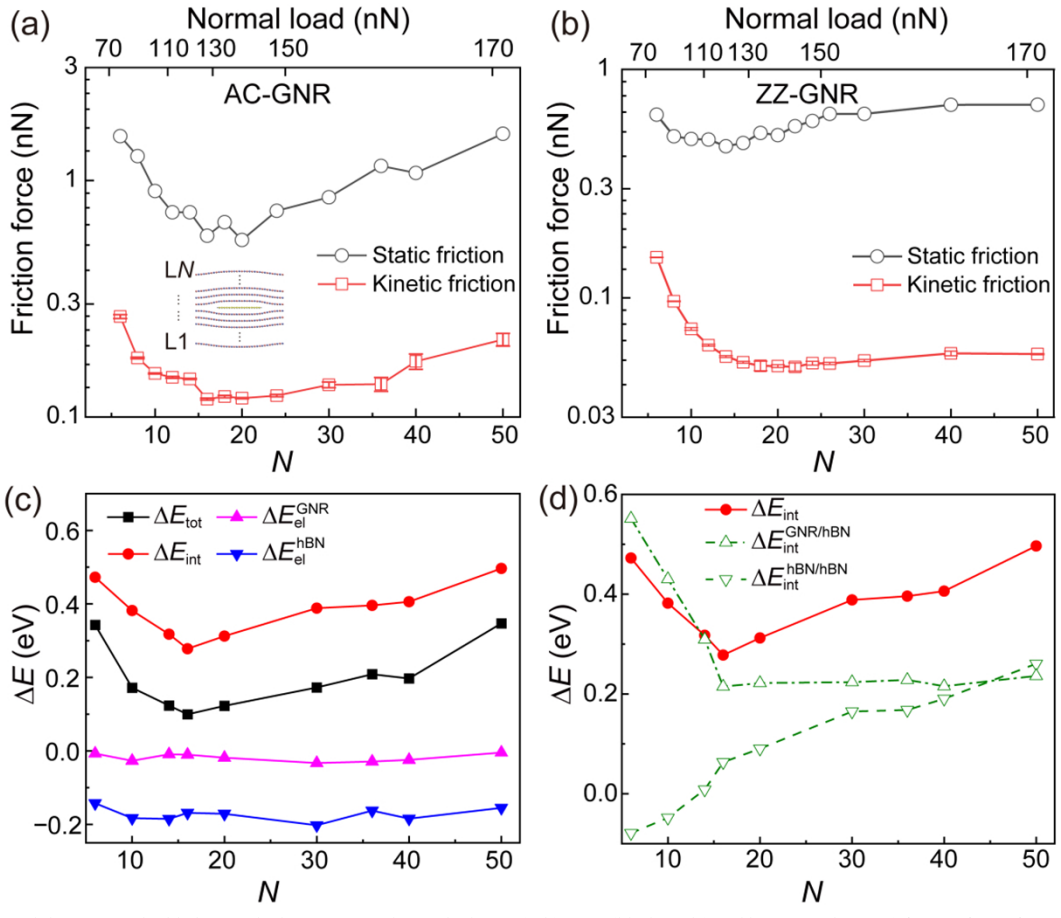

Fig. 4 Friction modulation in embedded GNRs by h-BN encapsulation thickness. (a, b) Static (black circle) and kinetic (red square) friction forces for embedded (a) AC-GNRs and (b) ZZ-GNRs as a function of the number of h-BN layers (N). The top axis indicates the corresponding normal load exerted by the encapsulation stack. The inset in (a) shows a side view of the simulation model. (c) Energy barrier of embedded AC-GNRs and their decomposition into the interlayer term (ΔE_{int}) and the intralayer elastic contributions from GNRs ($\Delta E_{\mathrm{el}}^{\mathrm{GNR}}$) and h-BN stack ($\Delta E_{\mathrm{el}}^{\mathrm{hBN}}$). (d) Further decomposition of ΔE_{int} into GNR/h-BN interfacial contributions ($\Delta E_{\mathrm{int}}^{\mathrm{GNR/hBN}}$) and h-BN/h-BN ($\Delta E_{\mathrm{int}}^{\mathrm{hBN/hBN}}$) interlayer interaction contributions.

increases friction, reaching ~0.21 nN (AC-GNR) and ~0.06 nN (ZZ-GNR) at 50 layers (with a vdW encapsulation normal load of ~175 nN). The corresponding differential friction coefficients (μ_k), obtained from a numerical two-point derivative of the kinetic friction with respect to the normal load, remain in nearly all cases within the superlubric regime ($\mu_k < 0.001$) [102], as shown in Fig. S25 in the ESM.

This non-monotonic trend results from competition between two opposing mechanisms. On the one hand, increased vdW pressure at higher N flattens the GNR by suppressing out-of-plane ripples induced by the ~1.8% lattice mismatch between GNR and h-BN [76, 96] (Fig. S26 in the ESM). This flattening reduces the variation in the GNR/h-BN interaction energy ($\Delta E_{\mathrm{int}}^{\mathrm{GNR/hBN}}$) during sliding, thereby lowering the total energy barrier (ΔE_{tot}) and friction. On the other hand, thicker h-BN stacks involve more h-BN/h-BN interlayer pairs perturbed during sliding, which monotonically increases the associated interaction energy variation ($\Delta E_{\mathrm{int}}^{\mathrm{hBN/hBN}}$) and raises ΔE_{tot} (Fig. S27 in the ESM). These mechanisms are quantified by decomposing ΔE_{tot}. While the elastic contributions from the GNR and h-BN remain nearly constant, the interlayer term ΔE_{int} mirrors the non-monotonic friction trend (Fig. 4(c)). Its components show opposing dependencies: $\Delta E_{\mathrm{int}}^{\mathrm{GNR/hBN}}$ decreases and then saturates with increasing N, whereas $\Delta E_{\mathrm{int}}^{\mathrm{hBN/hBN}}$ grows steadily (Fig. 4(d)). The critical role of ripple suppression is validated by constrained simulations in which GNR out-of-plane motion is prohibited; under this condition, friction increases monotonically with N (Fig. S28 in the ESM). Thus, the friction minimum at $N \approx 16$ marks the point where the reduction from ripple suppression is balanced by the increase from cumulative h-BN/h-BN perturbations.

The modulation of dynamic friction can be further clarified by examining how different energy dissipation channels evolve with the number of encapsulating h-BN layers (N). Figures 5(a) and 5(c) show that the total steady-state dissipation power ($\langle P \rangle$) shows the same nonmonotonic dependence on N as the friction force (Fig. S29 in the ESM). The dissipation is found to be dominated by the vertical component (red curves in Figs. 5(a) and 5(c), consistent with prior observations in periodic graphene/h-BN heterostructures [96], where the competition between moiré ridge suppression and narrowing under pressure led to similar load-dependent frictional trends. In our encapsulated GNR system, however, the underlying mechanism differs. Statistical analysis of the atomic dissipation for the 6, 16, and 50 h-BN layers (Figs. 5(b) and 5(d) and Figs. S30 and S31 in the ESM) shows that it follows a lognormal distribution function:

$$\rho(x) = \frac{A}{x\sigma\sqrt{2\pi}} \exp\left(-\frac{(\ln x - \mu)^2}{2\sigma^2}\right) \tag{6}$$

where $x = \langle p_{\mathrm{diss}}^{j} \rangle$, and A is an amplitude factor that scales the probability density function to match the histogram counts. μ and σ are the mean and the standard deviation of the distribution,

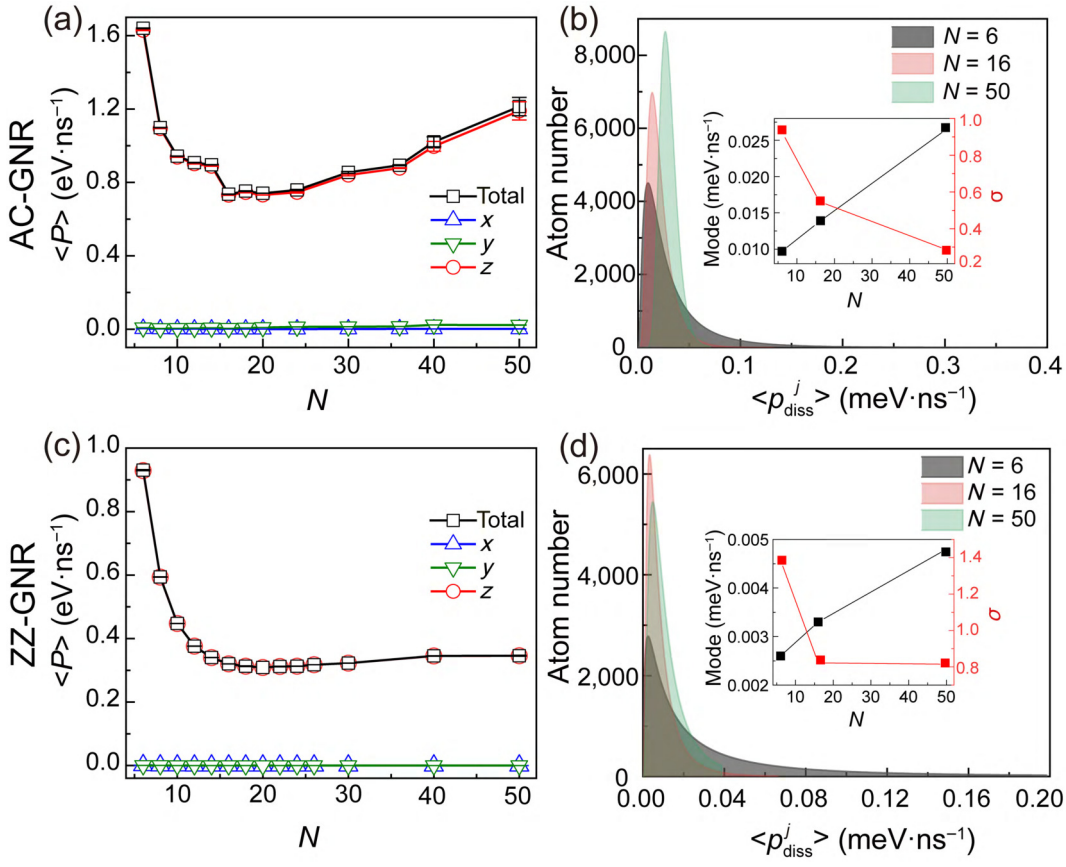

Fig. 5 Energy dissipation characteristics of embedded GNR systems as a function of the number of h-BN encapsulation layers. (a, c) Total steady-state dissipation power $\langle P \rangle$ and its directional components as a function of the number of h-BN layers. (b, d) Lognormal fits of static distributions of atomic energy dissipation power $\langle p_{\mathrm{diss}}^{j} \rangle$ for embedded GNR systems with 6, 16, and 50 h-BN layers. The insets in (b, d) show the evolution of the mode ($e^{\mu-\sigma^2}$) and the standard deviation (σ). (a, b) correspond to embedded AC-GNR systems, while (c, d) correspond to embedded ZZ-GNR systems.

respectively. The mode ($e^{\mu-\sigma^2}$) extracted from the distribution provides the most likely dissipation value.

The detailed fitting parameters are summarized in Table S2 in the ESM. As the number of encapsulating h-BN layers (N) increases, the dissipation distribution evolves in two key ways (Figs. 5(b) and 5(d) and Fig. S32 in the ESM). First, the high-dissipation tail is gradually suppressed, eliminating rare but extreme energy loss events. Second, the mode ($e^{\mu-\sigma^2}$) shifts upward, indicating that the baseline level of atomic dissipation becomes higher. These two opposing trends give rise to the observed valley-shaped dependence of friction on encapsulation thickness: Friction decreases at intermediate N due to the suppression of extreme events but increases again at large N as the elevated baseline dissipation begins to dominate. This evolution is closely tied to the out-of-plane dynamics of the GNR. At low confinement, the pronounced ripples trigger intermittent high-dissipation bursts (Movie S3 in the ESM). Thicker encapsulation clamps these ripples (Fig. S26 in the ESM), reducing dissipation. At very high N, however, the ribbon exhibits a rapid oscillatory out-of-plane fluctuation mode during sliding (Movie S4 in the ESM), which shifts the baseline dissipation upward and results in the eventual friction increase.

4 Conclusions

In summary, our MD simulations reveal that GNRs embedded within AA′-stacked h-BN layers exhibit friction more than an order of magnitude lower than their on-surface counterparts, with sublinear length scaling that persists without saturation up to hundreds of nanometers. The origin of this ultralow friction lies in registry competition at the encapsulated interfaces, which suppresses strain accumulation and stress localization, thereby enabling smooth collective sliding instead of soliton-mediated stick-slip. The friction can be further tuned by varying the encapsulation thickness, displaying a non-monotonic trend where a minimum occurs once the friction-reducing effect of pressure-induced ripple suppression balances the friction-increasing effect of cumulative h-BN/h-BN interlayer perturbations. These results clarify the microscopic origins of superlubricity in encapsulated vdW heterostructures and establish encapsulation as a practical approach for friction control. Beyond fundamental insight, this work offers guiding principles for designing robust, durable, and energy-efficient GNR-based nanoelectronic devices and scalable superlubric systems.

Acknowledgements

This work was supported by the National Natural Science Foundation of China (Nos. 12472099 and U2441207), the Fundamental Research Funds for the Central Universities (Nos. 2042025kf0050, 2042025kf0013, and 600460100), and the National Key Research and Development Program of China (2025YFF0513900, 2025YFF0513901). Computations were conducted at the Supercomputing Center of Wuhan University, the National Supercomputer TianHe-1(A) Center in Tianjin, and the Computing Center in Xi'an.

Author contributions

Wengen Ouyang conceived and supervised the project. Sen Wang

designed and performed the simulations. Both authors analyzed the data, interpreted the results, and wrote the manuscript.

Availability of data and materials

The data that support the findings of this study are available from the corresponding author upon reasonable request.

Competing interests

The authors have no competing interests to declare that are relevant to the content of this article.

Electronic Supplementary Material

Supplementary material (spring stiffness sensitivity test; optimized model of GNR/h-BN systems; periodicity of the lateral force traces; chirality-dependent friction mechanism of embedded GNRs; sliding velocity sensitivity test; temperature sensitivity test; robustness of ultralow friction and sublinear friction-length scaling against width and chiral geometry; definition of the axial GNR unit cell; stress, strain, bond-length, registry, and displacement evolution of on-surface and embedded GNRs; effect of interlayer interaction on friction differences; stress evolution for short on-surface; energy dissipation analysis and its morphological origins; encapsulation pressure in embedded GNR system; effect of h-BN thickness on friction coefficients and dynamics of embedded GNR; statistical analysis of energy dissipation of embedded GNRs; stress evolution of embedded GNRs during sliding (Movie S1); stress evolution of on-surface GNRs during sliding (Movie S2); out-of-plane fluctuation of embedded GNRs encapsulated by six h-BN layers (Movie S3); out-of-plane fluctuation of embedded GNRs encapsulated by fifty h-BN layers (Movie S4)) is available in the online version of this article at https://doi.org/10.26599/FRICT.2026.9441242.

References

[1] Yang L, Park C H, Son Y W, Cohen M L, Louie S G. Quasiparticle energies and band gaps in graphene nanoribbons. *Phys Rev Lett* **99** (18): 186801 (2007)

[2] Son Y W, Cohen M L, Louie S G. Energy gaps in graphene nanoribbons. *Phys Rev Lett* **97**(21): 216803 (2006)

[3] Lee C, Wei X D, Kysar J W, Hone J. Measurement of the elastic properties and intrinsic strength of monolayer graphene. *Science* **32 1**(5887): 385–388 (2008)

[4] Wang H M, Wang H S, Ma C X, Chen L X, Jiang C X, Chen C, Xie X M, Li A P, Wang X R. Graphene nanoribbons for quantum electronics. *Nat Rev Phys* **3**(12): 791–802 (2021)

[5] Radsar T, Khalesi H, Ghods V. Graphene nanoribbon field effect transistors analysis and applications. *Superlattices Microstruct* **153**: 106869 (2021)

[6] Wang H S, Chen L X, Elibol K, He L, Wang H M, Chen C, Jiang C X, Li C, Wu T R, Cong C X, et al. Towards chirality control of graphene nanoribbons embedded in hexagonal boron nitride. *Nat Mater* **20**(2): 202–207 (2021)

[7] Lone S, Bhardwaj A, Pandit A K, Gupta S, Mahajan S. A review of graphene nanoribbon field-effect transistor structures. *J Electron Mater* **50**(6): 3169–318 (2021)

[8] Kumar S, Pratap S, Kumar V, Mishra R K, Gwag J S, Chakraborty B. Electronic, transport, magnetic, and optical properties of graphene nanoribbons and their optical sensing applications: A comprehensive review. *Luminescence* **38**(7): 909–953 (2023)

[9] Wei T Y, Li H, Fu Y M, Zheng X X, Huang L, Song A M. A graphene-nanoribbon-based thermoelectric generator. *Carbon* **210**: 118053 (2023)

[10] Dinh C, Yusufoglu M, Yumigeta K, Kinikar A, Sweepe T, Zeszut Z, Chang Y J, Copic C, Janssen S, Holloway R, et al. Atomically precise graphene nanoribbon transistors with long-term stability and reliability. *ACS Nano* **18**(34): 22949–22957 (2024)

[11] Zhang J, Calame M, Perrin M L. Contacting atomically precise graphene nanoribbons for next-generation quantum electronics. *Matter* **5**(8): 2497–2499 (2022)

[12] Li X L, Wang X R, Zhang L, Lee S, Dai H J. Chemically derived, ultrasmooth graphene nanoribbon semiconductors. *Science* **319** (5867): 1229–1232 (2008)

[13] Xu W T, Seo H K, Min S Y, Cho H, Lim T S, Oh C Y, Lee Y, Lee T W. Rapid fabrication of designable large-scale aligned graphene nanoribbons by electro-hydrodynamic nanowire lithography. *Adv Mater* **26**(21): 3459–3464 (2014)

[14] Jiao L Y, Wang X R, Diankov G, Wang H L, Dai H J. Facile synthesis of high-quality graphene nanoribbons. *Nat Nanotechnol* **5** (5): 321–325 (2010)

[15] Kim K, Sussman A, Zettl A. Graphene nanoribbons obtained by electrically unwrapping carbon nanotubes. *ACS Nano* **4**(3): 1362–1366 (2010)

[16] Chen L X, He L, Wang H S, Wang H M, Tang S J, Cong C X, Xie H, Li L, Xia H, Li T X, et al. Oriented graphene nanoribbons embedded in hexagonal boron nitride trenches. *Nat Commun* **8**: 14703 (2017)

[17] Way A J, Jacobberger R M, Arnold M S. Seed-initiated anisotropic growth of unidirectional armchair graphene nanoribbon arrays on germanium. *Nano Lett* **18**(2): 898–906 (2018)

[18] Cai L, He W Z, Xue X D, Huang J Y, Zhou K, Zhou X H, Xu Z P, Yu G. *In situ* growth of large-area and self-aligned graphene nanoribbon arrays on liquid metal. *Natl Sci Rev* **8**(12): nwaa298 (2021)

[19] Way A J, Jacobberger R M, Guisinger N P, Saraswat V, Zheng X Q, Suresh A, Dwyer J H, Gopalan P, Arnold M S. Graphene nanoribbons initiated from molecularly derived seeds. *Nat Commun* **13**(1): 2992 (2022)

[20] Zou M Z, Liu W M, Yu Y, Wang S S, Xu B, Qian L, Tong T Z, Zhang J. Direct growth of globally aligned graphene nanoribbons on reconstructed sapphire substrate using PECVD. *Nano Res* **16**(1): 62–69 (2023)

[21] Lyu B S, Chen J J, Lou S, Li C, Qiu L, Ouyang W, Xie J X, Mitchell I, Wu T Y, Deng A L, et al. Catalytic growth of ultralong graphene nanoribbons on insulating substrates. *Adv Mater* **34**(28): 2200956 (2022)

[22] Cai J M, Ruffieux P, Jaafar R, Bieri M, Braun T, Blankenburg S, Muoth M, Seitsonen A P, Saleh M, Feng X L, et al. Atomically precise bottom-up fabrication of graphene nanoribbons. *Nature* **46 6**(7305): 470–473 (2010)

[23] Sakaguchi H, Song S T, Kojima T, Nakae T. Homochiral polymerization-driven selective growth of graphene nanoribbons. *Nat Chem* **9**(1): 57–63 (2017)

[24] Kolmer M, Steiner A K, Izydorczyk I, Ko W, Engelund M, Szymonski M, Li A P, Amsharov K. Rational synthesis of atomically precise graphene nanoribbons directly on metal oxide surfaces. *Science* **369**(6503): 571–575 (2020)

[25] Luo H, Yu G. Preparation, bandgap engineering, and performance control of graphene nanoribbons. *Chem Mater* **34**(8): 3588–3615 (2022)

[26] Saraswat V, Jacobberger R M, Arnold M S. Materials science challenges to graphene nanoribbon electronics. *ACS Nano* **15**(3): 3674–3708 (2021)

[27] Koen Houtsma R S, de la Rie J, Stöhr M. Atomically precise graphene nanoribbons: Interplay of structural and electronic properties. *Chem Soc Rev* **50**(11): 6541–6568 (2021)

[28] Lyu B S, Chen J J, Wang S, Lou S, Shen P Y, Xie J X, Qiu L, Mitchell I, Li C, Hu C, et al. Graphene nanoribbons grown in hBN stacks for high-performance electronics. *Nature* **628**(8009): 758–764 (2024)

[29] Shen P Y, Lyu B S, Wang L G, Zhang Z C, Zhou X L, Lou S, Chen J J, Ma S Q, Xie Y F, Chen Y, et al. Coulomb blockade and possible luttinger liquid behaviors in encapsulated high-mobility graphene nanoribbons. *Nano Lett* **25**(22): 8825–8833 (2025)

[30] Yi H, Solís-Fernández P, Lin Y C, Suenaga K, Ago H. Bottom-up confined synthesis of air-stable two-dimensional SnS and SnS_2 between hexagonal boron nitride nanosheets. *ACS Appl Nano Mater* **8**(6): 2693–2700 (2025)
[31] Hu J, Yu Z, Yang Y, Huang J X, Liu Z Y, Huang S, Wang M, Yang H. Graphene nanoribbon core thermotropic liquid crystal with a well-defined molecular structure. *Angew Chem Int Edit* **64**(21): 202501161 (2025)
[32] Li Z J, Zhang Z, Lu J. Van der Waals gap engineering of emergent two-dimensional materials. *Acc Mater Res* **6**(1): 52–63 (2025)
[33] Verzhbitskiy I A, Mishra A, Mitra S, Zhang Z P, Das S, Lau C S, Lee R, Huang D, Eda G, Ang Y S, et al. Low-temperature contacts and the coulomb blockade effect in layered nanoribbons with in-plane anisotropy. *ACS Nano* **19**(11): 10878–10888 (2025)
[34] Zhu H, Wen G Z, Zheng W H, Rees N H, Stawski W, Wang H I, Bonn M, Anderson H L. High charge carrier mobility in porphyrin nanoribbons. *Angew Chem Int Edit* **137**(6): 202417429 (2025)
[35] Kawai S, Benassi A, Gnecco E, Söde H, Pawlak R, Feng X L, Müllen K, Passerone D, Pignedoli C A, Ruffieux P, et al. Superlubricity of graphene nanoribbons on gold surfaces. *Science* **351**(6276): 957–961 (2016)
[36] Gigli L, Manini N, Benassi A, Tosatti E, Vanossi A, Guerra R. Graphene nanoribbons on gold: Understanding superlubricity and edge effects. *2D Mater* **4**(4): 045003 (2017)
[37] Gigli L, Manini N, Tosatti E, Guerra R, Vanossi A. Lifted graphene nanoribbons on gold: From smooth sliding to multiple stick-slip regimes. *Nanoscale* **10**(4): 2073–2080 (2018)
[38] Xue Z M, Chen G B, Wang C G, Huang R. Peeling and sliding of graphene nanoribbons with periodic van der Waals interactions. *J Mech Phys Solids* **158**: 104698 (2022)
[39] Ouyang W G, Hod O, Urbakh M. Registry-dependent peeling of layered material interfaces: The case of graphene nanoribbons on hexagonal boron nitride. *ACS Appl Mater Inter* **13**(36): 43533–43539 (2021)
[40] Li R Y, Cong Y, Xu F. Tunable tail swing of nanomillipedes. *Nano Lett* **23**(23): 10879–10883 (2023)
[41] Yu J, Han E, Hossain M A, Watanabe K, Taniguchi T, Ertekin E, van der Zande A M, Huang P Y. Designing the bending stiffness of 2D material heterostructures. *Adv Mater* **33**(9): 2007269 (2021)
[42] Han E, Yu J, Annevelink E, Son J, Kang D A, Watanabe K, Taniguchi T, Ertekin E, Huang P Y, van der Zande A M. Ultrasoft slip-mediated bending in few-layer graphene. *Nat Mater* **19**(3): 305–309 (2020)
[43] Zhang B D, Qiu W, Liao X B, He L H, Ni Y. Impact of out-of-plane deformation on atomic reconstruction in twisted van der Waals bilayers. *J Mech Phys Solids* **189**: 105693 (2024)
[44] Chen Z, Kim S H. Measuring nanoscale friction at graphene step edges. *Friction* **8**(4): 802–811 (2020)
[45] Chen Z, Khajeh A, Martini A, Kim S H. Identifying physical and chemical contributions to friction: A comparative study of chemically inert and active graphene step edges. *ACS Appl Mater Inter* **12**(26): 30007–30015 (2020)
[46] Li Y T, He W J, He Q C, Wang W. Contributions of edge and internal atoms to the friction of two-dimensional heterojunctions. *Phys Rev Lett* **133**(12): 126202 (2024)
[47] Wang H, Wang S, Zhang S, Zhu M Z, Ouyang W G, Li Q Y. Deducing the internal interfaces of twisted multilayer graphene via Moiré-regulated surface conductivity. *Natl Sci Rev* **10**(8): nwad175 (2023)
[48] Nahid S M, Nam S, van der Zande A M. Depolarization field-induced photovoltaic effect in graphene/α-In_2Se_3/graphene heterostructures. *ACS Nano* **18**(22): 14198–14206 (2024)
[49] Xu B, Deng J K, Ding X D, Sun J, Liu J Z. Van der Waals force-induced intralayer ferroelectric-to-antiferroelectric transition via interlayer sliding in bilayer group-IV monochalcogenides. *Npj Comput Mater* **8**(1): 47 (2022)
[50] Zhang S, Xu Q, Hou Y, Song A S, Ma Y, Gao L, Zhu M Z, Ma T B, Liu L Q, Feng X Q, et al. Domino-like stacking order switching in twisted monolayer-multilayer graphene. *Nat Mater* **21**(6): 621–626 (2022)
[51] Ouyang W G, Qin H S, Urbakh M, Hod O. Controllable thermal conductivity in twisted homogeneous interfaces of graphene and hexagonal boron nitride. *Nano Lett* **20**(10): 7513–7518 (2020)
[52] Jiang W W, Liang T, Xu J B, Ouyang W G. Twist-dependent anisotropic thermal conductivity in homogeneous MoS_2 stacks. *Int J Heat Mass Tran* **217**: 124662 (2023)
[53] Jiang W W, Liang T, Xu J B. Moiré-driven interfacial thermal transport in twisted transition metal dichalcogenides. *ACS Nano* **19**(17): 16287–16296 (2025)
[54] Kim S E, Mujid F, Rai A, Eriksson F, Suh J, Poddar P, Ray A, Park C, Fransson E, Zhong Y, et al. Extremely anisotropic van der Waals thermal conductors. *Nature* **597**(7878): 660–665 (2021)
[55] Jiang W W, Liang T, Xu J B, Ouyang W G. Strain-engineered anisotropic thermal transport in layered MoS_2 structures. *ACS Appl Mater Inter* **17**(23): 34833–34844 (2025)
[56] de Wijn A S, Fasolino A, Filippov A E, Urbakh M. Nanoscopic friction under electrochemical control. *Phys Rev Lett* **112**(5): 055502 (2014)
[57] Wu Z H, Wu T L, Xiang X J, Chen W P, Wang Y, Yang D L, Tang D C, Liu Y, An J, Nie J H, et al. Ultralow resistivity of the graphite/Au van der Waals heterostructure in the structural superlubric state. *Nano Lett* **24**(48): 15481–15487 (2024)
[58] Wang Y, Wang J, Wu T L, Chen W P, Peng D L, Wu Z H, Ma M, Zheng Q S. The anomalous effect of electric field on friction for microscale structural superlubric graphite/Au contact. *Natl Sci Rev* **11**(9): nwae019 (2024)
[59] Yang F W, Zhou W J, Zhang Z B, Huang X Y, Zhang J W, Liang N J, Yan W J, Wang Y X, Ding M C, Guo Q L, et al. Ultrahigh thermal conductance across superlubric interfaces in twisted graphite. *Phys Rev Lett* **134**(14): 146302 (2025)
[60] Liao M Z, Cammarata A, Polcar T. Charge-induced ultralow friction between graphite and atomically flat surfaces. *Carbon* **223**: 119036 (2024)
[61] Song A S, Shi R Y, Lu H L, Wang X Y, Hu Y Z, Gao H J, Luo J B, Ma T B. Fluctuation of interfacial electronic properties induces friction tuning under an electric field. *Nano Lett* **22**(5): 1889–1896 (2022)
[62] Li Z W, Lv Y W, Ren L W, et al. Efficient strain modulation of 2D materials via polymer encapsulation. *Nat Commun* **11**: 1151 (2020)
[63] Li P P, Ju P F, Ji L, Li H X, Liu X H, Chen L, Zhou H D, Chen J M. Toward robust macroscale superlubricity on engineering steel substrate. *Adv Mater* **32**(36): 2002039 (2020)
[64] Katiyar A K, Hoang A T, Xu D, Hong J, Kim B J, Ji S, Ahn J H. 2D materials in flexible electronics: Recent advances and future prospectives. *Chem Rev* **124**(2): 318–419 (2024)
[65] Peng D L, Wang J, Jiang H Y, Zhao S J, Wu Z H, Tian K W, Ma M, Zheng Q S. 100 km wear-free sliding achieved by microscale superlubric graphite/DLC heterojunctions under ambient conditions. *Natl Sci Rev* **9**(1): nwab109 (2022)
[66] Wang Y. , Yang X, Liang H, Zhao J, Zhang J. Macroscale superlubricity on nanoscale graphene Moiré structure-assembled surface via counterface hydrogen modulation. *Adv Sci* **11**(19): 2309701 (2024).
[67] Ouyang W, Mandelli D, Urbakh M, Hod O. Nanoserpents: Graphene nanoribbon motion on two-dimensional hexagonal materials. *Nano Lett* **18**(9): 6009–6016 (2018).
[68] Gao X, Ouyang W, Kronik L, Urbakh M, Hod O. Anisotropic interlayer force fields for van der Waals interfaces: Development and applications. *J Chem Phys* **163**(4): 041001 (2025).
[69] Brenner D W, Shenderova O A, Harrison J A, Stuart S J, Ni B, Sinnott S B. A second-generation reactive empirical bond order (REBO) potential energy expression for hydrocarbons. *J Phys-Condens Mat* **14**(4): 783–802 (2002)
[70] Kınacı A, Haskins J B, Sevik C, Çağın T. Thermal conductivity of BN-C nanostructures. *Phys Rev B* **86**(11): 115410 (2012)

[71] Ouyang W G, Azuri I, Mandelli D, Tkatchenko A, Kronik L, Urbakh M, Hod O. Mechanical and tribological properties of layered materials under high pressure: Assessing the importance of many-body dispersion effects. *J Chem Theory Comput* **16**(1): 666–676 (2020)
[72] Jiang W W, Sofer R, Gao X, Tkatchenko A, Kronik L, Ouyang W, Urbakh M, Hod O. Anisotropic interlayer force field for group-VI transition metal dichalcogenides. *J Phys Chem A* **127**(46): 9820–9830 (2023)
[73] Yao Y P, Wu B Z, Liu Z, Ouyang W G. Semianisotropic interfacial potential for interfaces between metal and 2D carbon allotrope. *J Phys Chem C* **128**(16): 6836–6851 (2024)
[74] Jiang W W, Sofer R, Gao X, Kronik L, Hod O, Urbakh M, Ouyang W G. Anisotropic interlayer force field for heterogeneous interfaces of graphene and h-BN with transition metal dichalcogenides. *J Phys Chem C* **129**(2): 1417–1427 (2025)
[75] Vizner Stern M, Waschitz Y, Cao W, Nevo I, Watanabe K, Taniguchi T, Sela E, Urbakh M, Hod O, Ben Shalom M. Interfacial ferroelectricity by van der Waals sliding. *Science* **372**(6549): 1462–1466 (2021)
[76] Ouyang W, Hod O, Urbakh M. Parity-dependent Moiré superlattices in graphene/hBN heterostructures: A route to mechanomutable metamaterials. *Phys Rev Lett* **126**(21): 216101 (2021)
[77] Yao Y P, Song Y M, Wu B Z, Scherb S, Huang S Y, Hinaut A, Glatzel T, Meyer E, Liu Z, Ouyang W G. Unraveling the interfacial properties of twisted single-crystal Au(111)/MoS_2 heterostructures: A pathway to robust superlubricity. *Adv Sci* **12**(21): 2415884 (2025)
[78] Huang K, Qin H S, Zhang S, Li Q Y, Ouyang W G, Liu Y L. The origin of Moiré-level stick-slip behavior on graphene/h-BN heterostructures. *Adv Funct Mater* **32**(35): 2204209 (2022)
[79] Zhang Z C, Chen Y, Shen P Y, Chen J J, Wang S, Wang B, Ma S Q, Lyu B S, Zhou X L, Lou S, et al. Homochiral carbon nanotube van der Waals crystals. *Science* **387**(6740): 1310–1316 (2025)
[80] Bu H K, Jiang W W, Ying P H, Liang T, Fan Z Y, Ouyang W G. Modular hybrid machine learning and physics-based potentials for scalable modeling of van der Waals heterostructures. *J Mech Phys Solids* **210**: 106540 (2026)
[81] Thompson A P, Aktulga H M, Berger R, Bolintineanu D S, Brown W M, Crozier P S, In't Veld P J, Kohlmeyer A, Moore S G, Nguyen T D, et al. LAMMPS—A flexible simulation tool for particle-based materials modeling at the atomic, meso, and continuum scales. *Comput Phys Commun* **271**: 108171 (2022)
[82] Wang J, Ma M, Tosatti E. Kinetic friction of structurally superlubric 2D material interfaces. *J Mech Phys Solids* **180**: 105396 (2023).
[83] Kantorovich L. Generalized Langevin equation for solids. I. Rigorous derivation and main properties. *Phys Rev B* **78**(9): 094304 (2008)
[84] Kantorovich L, Rompotis N. Generalized Langevin equation for solids. II. Stochastic boundary conditions for nonequilibrium molecular dynamics simulations. *Phys Rev B* **78**(9): 094305 (2008)
[85] Benassi A, Vanossi A, Santoro G E, Tosatti E. Optimal energy dissipation in sliding friction simulations. *Tribol Lett* **48**(1): 41–49 (2012)
[86] Yan W D, Gao X, Ouyang W G, Liu Z, Hod O, Urbakh M. Shape-dependent friction scaling laws in twisted layered material interfaces. *J Mech Phys Solids* **185**: 105555 (2024)
[87] de Oteyza D G, García-Lekue A, Vilas-Varela M, Merino-Díez N, Carbonell-Sanromà E, Corso M, Vasseur G, Rogero C, Guitián E, Pascual J I, et al. Substrate-independent growth of atomically precise chiral graphene nanoribbons. *ACS Nano* **10**(9): 9000–9008 (2016)
[88] Li J C, Sanz S, Merino-Díez N, Vilas-Varela M, Garcia-Lekue A, Corso M, de Oteyza D G, Frederiksen T, Peña D, Pascual J I. Topological phase transition in chiral graphene nanoribbons: From edge bands to end states. *Nat Commun* **12**(1): 5538 (2021)
[89] Hod O. Quantifying the stacking registry matching in layered materials. *Isr J Chem* **50**(4): 506–514 (2010)
[90] Leven I, Krepel D, Shemesh O, Hod O. Robust Superlubricity in graphene/h-BN heterojunctions. *J Phys Chem Lett* **4**(1): 115–120 (2013)
[91] Ji J C, Yu M L, Guo W L, Chen C F, Zhang Z H. Strain soliton activated gliding for length invariant friction. *Nano Lett* **25**(21): 8789–8795 (2025)
[92] Feng S Z, Xu Z P. Robustness of structural superlubricity beyond rigid models. *Friction* **10**(9): 1382–1392 (2022)
[93] Dong Y, Wang Y K, Duan Z Q, Huang S Y, Tao Y, Lu X, Zhang Y, Kan Y J, Wei Z Y, Li D Y, et al. Phononic origin of structural lubrication. *Friction* **11**(6): 966–976 (2023)
[94] Dong Y, Hui W B, Lian F M, Ding Y S. Phononic origin of strain-controlled friction force. *Tribol Int* **184**: 108474 (2023)
[95] Wei Z Y, Xiang L, Kan Y J, Zhang Y, Chen Y F. Effects of the normal load on the excited phonons in atomic friction. *J Appl Phys* **132**(17): 175301 (2022)
[96] Mandelli D, Ouyang W, Hod O, Urbakh M. Negative friction coefficients in superlubric graphite–hexagonal boron nitride heterojunctions. *Phys Rev Lett* **122**(7): 076102 (2019).
[97] Gao X, Yan W D, Ouyang W, Liu Z, Urbakh M, Hod O. Frictional dissipation and scaling laws at van der Waals interfaces: The role of edge and corner elastic Moiré pinning. *ACS Nano* **19**(32): 29255–29264 (2025)
[98] Algara-Siller G, Lehtinen O, Wang F C, Nair R R, Kaiser U, Wu H A, Geim A K, Grigorieva I V. Square ice in graphene nanocapillaries. *Nature* **519**(7544): 443–445 (2015)
[99] Khestanova E, Guinea F, Fumagalli L, Geim A K, Grigorieva I V. Universal shape and pressure inside bubbles appearing in van der Waals heterostructures. *Nat Commun* **7**: 12587 (2016)
[100] Vasu K S, Prestat E, Abraham J, Dix J, Kashtiban R J, Beheshtian J, Sloan J, Carbone P, Neek-Amal M, Haigh S J, et al. Van der Waals pressure and its effect on trapped interlayer molecules. *Nat Commun* **7**(1): 12168 (2016)
[101] Hu C, Chen J, Zhou X, Xie Y, Huang X, Wu Z, Ma S, Zhang Z, Xu K, Wan N, Zhang Y, Liang Q, Shi Z. Collapse of carbon nanotubes due to local high-pressure from van der Waals encapsulation. *Nat Commun* **15**(1): 3486 (2024)
[102] Erdemir A, Martin J M. *Superlubricity*. Amsterdam (the Netherlands): Elsevier, 2007.

Sen Wang received his B.Eng. (2016) and M.Eng. (2019) degrees in engineering mechanics from Dalian University of Technology, China. He is currently a Ph.D. candidate in the Department of Engineering Mechanics, School of Civil Engineering, Wuhan University, China. His research interests focus on the mechanical, electrical, and tribological behaviors of van der Waals interfaces.

Wengen Ouyang received his B.Sc. degree in 2011 from Wuhan University, China, and his Ph.D. degree in 2016 from Tsinghua University, China. He then carried out postdoctoral research at Tel Aviv University, Israel. Since 2021, he has worked as a full professor in the Department of Engineering Mechanics at Wuhan University, China. His research interests focus on surface/interface mechanics and computational tribology. The computational methods he developed for van der Waals interfaces have been incorporated into the widely used open-source molecular dynamics software packages LAMMPS and GPUMD.